INORGANIC CHEMISTRY FRONTIERS

CHINESE CHEMICAL SOCIETY ROYAL SOCIETY OF CHEMISTRY

RESEARCH ARTICLE

View Article Online
View Journal | View Issue

Check for updates

Cite this: *Inorg. Chem. Front.*, 2025, **12**, 2439

Multiple interface coupling triggered built-in electric field over double-sandwiched RGO/cobalt silicate/cobalt-iron phosphide for improving the overall water-splitting performance†

Yifu Zhang, *[a,b] Xianfang Tan,[a] Xiaoyu Pei,[b] Yang Wang,[b] Shengping Yi,[c] Qiushi Wang,*[d] Xiaoming Zhu,[a] Changgong Meng [b] and Chi Huang *[c]

Received 22nd November 2024,
Accepted 23rd January 2025

DOI: 10.1039/d4qi02987a

rsc.li/frontiers-inorganic

The exploration of efficient and durative bifunctional electrocatalysts for overall water splitting (OWS) is critical for hydrogen production in clean energy applications. Herein, a novel double-sandwiched architecture of reduced graphene oxide (rGO), cobalt silicate (CS), and cobalt–iron phosphides, denoted as rGO/CS/$(Co,Fe)_xP_y$, is designed to enhance both the oxygen evolution reaction (OER) and hydrogen ER (HER) in alkaline media. The formation of Co_2P and Fe_2P on rGO/CS not only protects the silicate from alkaline corrosion, but also generates dual-active centers that synergistically improve the conductivity and catalytic activity. Multiple interface coupling between rGO, CS, and $(Co,Fe)_xP_y$ triggers a built-in electric field, which significantly enhances charge separation, electron transport, and reaction kinetics. This built-in electric field lowers the energy barrier for HER by facilitating H–OH bond dissociation and accelerates the OER by promoting OH^- adsorption. The rGO/CS/$(Co,Fe)_xP_y$ catalyst achieves overpotentials of 256 mV (OER) and 180 mV (HER) at 10 mA cm^{-2}, surpassing most reported catalysts and rivaling commercial Pt/C and RuO_2. Furthermore, the rGO/CS/$(Co,Fe)_xP_y$ (+/−) demonstrates a low OWS voltage of 1.41 V. The current work provides a new approach to catalyst design through interface engineering and electric field optimization, offering a scalable solution for sustainable hydrogen production.

1. Introduction

Electrochemical water splitting (EWS) is a crucial technology for producing hydrogen, a clean and sustainable energy carrier that holds immense potential for revolutionizing the global energy system.[1–5] Among various water-splitting methods, alkaline water splitting is particularly attractive for industrial applications due to its safety, extended operational lifespan, and scalability.[6–9] However, the efficiency of this process is hindered by the slow kinetics of the oxygen evolution reaction (OER) and hydrogen evolution reaction (HER), both of which require highly efficient electrocatalysts to overcome significant energy barriers.[10–12] Developing low-cost, bifunctional catalysts capable of driving both the OER and HER in alkaline media is an urgent need for realizing practical overall water splitting (OWS).[13–15] Traditionally, noble metal-based catalysts like IrO_2 for OER and Pt/C for HER have been widely used due to their superior catalytic properties.[16] However, their high cost and limited availability pose significant obstacles to large-scale implementation.[17] This has driven research toward finding Earth-abundant and cost-effective alternatives that can efficiently catalyze both reactions. Recently, cobalt silicate (CS) has emerged as a promising non-precious metal catalyst, particularly for OER, due to its stable structure and moderate catalytic activity.[18–25] Despite these advantages, cobalt silicate faces drawbacks, including poor electrical conductivity and limited exposure of active sites, which hinder its effectiveness in OWS.[26] Moreover, under alkaline conditions, silicates are prone to degradation due to base-induced corrosion, which compromises their structural integrity and catalytic performance.[27,28]

Therefore, designing and synthesizing cobalt silicate-based catalysts that are stable and active in alkaline environments remain a substantial challenge. Unlike silicates, transition metal phosphides (TMPs) exhibit metallic properties that can greatly improve the conductivity of silicate-based materials.[29]

---

[a] *Hubei Key Laboratory of Radiation Chemistry and Functional Materials, School of Nuclear Technology and Chemistry & Biology, Hubei University of Science and Technology, Xianning 437100, China. E-mail: yfzhang@dlut.edu.cn*

[b] *School of Chemistry, Dalian University of Technology, Dalian 116024, China*

[c] *College of Chemistry and Molecular Sciences, Wuhan University, Wuhan 430072, China. E-mail: chihuang@whu.edu.cn*

[d] *School of Physics and Materials Engineering, Dalian Minzu University, Dalian 116600, P. R. China. E-mail: wangqiushi@dlnu.edu.cn*

† Electronic supplementary information (ESI) available. See DOI: **https://doi.org/10.1039/d4qi02987a**

After conversion to phosphides, the stability and intrinsic activity of the catalyst under alkaline conditions can be significantly enhanced. For instance, cobalt phosphide (Co_2P) has shown excellent performance in the HER,[30,31] primarily due to its ability to promote water dissociation, and iron phosphide (Fe_2P) has been effective in catalyzing the OER by facilitating the adsorption and conversion of oxygen intermediates.[32,33] However, the potential synergistic effects of combining cobalt silicate with transition metal phosphides (such as Co_2P and Fe_2P) to address both OER and HER challenges have not yet been fully explored.

A key innovation in this work is the creation of a built-in electric field triggered by interface coupling between the different components.[34] This built-in electric field plays a pivotal role in enhancing the overall catalytic performance of the material.[35] At the molecular level, interactions between conductive species (such as rGO and TMPs) and catalytically active sites (such as Co_2P and Fe_2P) create electronic gradients across the interfaces, resulting in the formation of a localized electric field.[36] Density functional theory (DFT) calculations reveal that this electric field facilitates both charge separation and transfer during water splitting.[37] Specifically, in the HER, the built-in electric field enhances the Volmer step, which involves the adsorption and dissociation of water molecules. By polarizing the H–OH bond, the electric field lowers the energy barrier for water dissociation, allowing hydrogen atoms to be more easily adsorbed onto the CoP active sites, thus accelerating the reaction kinetics.[38] For OER, the electric field promotes the adsorption of OH^- ions on the surface of the rGO/CS composite, leading to more efficient formation of oxygen intermediates (*e.g.*, *O, *OH) and their conversion into molecular oxygen, thereby improving OER kinetics.[23]

In this study, we successfully prepared a novel double-sandwiched electrochemical catalyst composed of rGO, CS, and $(Co,Fe)_xP_y$, with the aim of enhancing the OWS efficiency through interfacial coupling and synergistic effects. The *in situ* formation of CoP and FeP not only effectively protects the cobalt silicate from degradation in alkaline environments, but also establishes dual-active centers that enhance both conductivity and ionic transport. The built-in electric field generated between these centers improves the availability of active electrons for both OER and HER. This synergistic interaction is further amplified by the role of the rGO substrate, which uniformly distributes the electric field and facilitates efficient charge transfer across the composite structure. As a result, the rGO/CS/$(Co,Fe)_xP_y$ catalyst achieves the lowest η of 256 mV (OER) and 180 mV (HER) at 10 mA cm^{-2}, outperforming most reported OER and HER electrocatalysts based on transition metal silicates and other materials (Tables S2 and S3†), and even rivaling commercial RuO_2 and Pt/C catalysts.[24] Additionally, the cell voltage for OWS using rGO/CS/$(Co,Fe)_xP_y$ (+/−) as both the anode and cathode is 1.41 V at 10 mA cm^{-2}, which surpasses many recently developed bifunctional catalysts and is superior to the traditional Pt/C||RuO_2 system.[24] This work contributes significantly to the understanding of interface engineering in electrocatalysis, offering new insights into how built-in electric fields and synergistic interactions between dual-active centers can enhance the catalytic efficiency. Furthermore, it provides both a theoretical and practical foundation for developing the next generation of bifunctional catalysts for sustainable and scalable hydrogen production through OWS.

2. Results and discussion

Fig. 1 illustrates the synthetic route for the target sample, rGO/CS/$(Co,Fe)_xP_y$, which is based on the rGO/CS composite.[39] Its detailed synthesis can be found in the ESI.† The SEM images in Fig. S1 (ESI†) show a sandwich-like structure with CS nanosheets grown on both sides of the rGO layers. The preparation of rGO/CS/$(Co,Fe)_xP_y$ involves three main steps: *in situ* growth of Co-MOF, iron ion exchange, and phosphating heat treatment. First, Co-MOF is *in situ* grown on the rGO/CS structure to form the rGO/CS/Co-MOF composite. The large surface area of rGO/CS enables efficient Co^{2+} adsorption, facilitating the nucleation and growth of Co-MOF on the rGO/CS surface. Compared to the pure Co-MOF (Fig. S2, ESI†), the Co-MOF in the rGO/CS/Co-MOF composite appears much smaller (Fig. 2a and Fig. S3, ESI†). The surface of rGO/CS/Co-MOF is densely coated with Co-MOF, distinct from the honeycomb-like nanosheets of the CS layer in rGO/CS. Next, an iron ion exchange process is conducted to synthesize iron-substituted rGO/CS/Co-MOF, which is denoted as rGO/CS/Co,Fe-MOF. During this step, the rGO/CS/Co-MOF composite is immersed in a solution containing Fe^{2+} ions, ethanol (CH_3CH_2OH), and water. This triggers ion exchange and partial etching of the Co-MOF, converting it into an amorphous Co–Fe compound (rGO/CS/Co,Fe-MOF), facilitated by the reversible hydrolysis of Fe^{2+} ($Fe^{2+} + 2H_2O \leftrightarrow Fe(OH)_2 + 2H^+$).[40] Then, the Co^{2+} ions react with iron hydroxide to form the Co,Fe-MOF structure. SEM analysis (Fig. 2b) shows that the Co-MOF nanoparticles are transformed into nanosheet-like Co,Fe-compounds, further confirming the successful ion exchange and conversion process. Finally, the rGO/CS/$(Co,Fe)_xP_y$ composite is obtained through a phosphating process. The rGO/CS/Co,Fe-MOF sample is treated with a phosphorus source at elevated temperatures in an inert atmosphere, resulting in the formation of Co,Fe-phosphide ($(Co,Fe)_xP_y$) nanoparticles. SEM images (Fig. 2c, d and Fig. S4, ESI†) clearly show that the rGO/CS/$(Co,Fe)_xP_y$ structure maintains the sandwich-like architecture (Fig. S3†),[41] with nanosheets of $(Co,Fe)_xP_y$ scattered across the rGO/CS surface. The morphology of the rGO/CS support is preserved, and the stacked intercalated structure consisting of the rGO/CS carrier and $(Co,Fe)_xP_y$ phosphide layers is evident. Elemental mapping by energy-dispersive X-ray spectroscopy (EDS) further confirms the formation of the rGO/CS/$(Co,Fe)_xP_y$ composite. Fig. S5–S7 (ESI†), along with Fig. 2e, show the distribution of elements in the different stages of synthesis. The initial rGO/CS contained carbon (C), oxygen (O), silicon (Si), and cobalt (Co) (Fig. S5†). After ion exchange, the rGO/CS/Co,Fe-MOF included iron (Fe) (Fig. S6†). Finally, the rGO/CS/(Co,

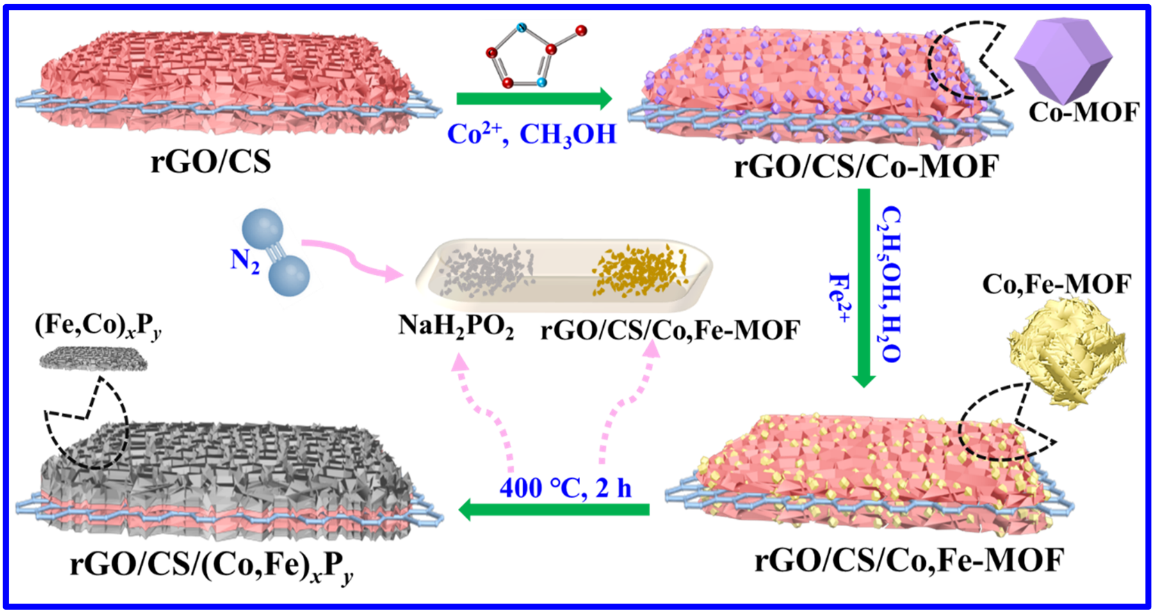

Fig. 1 Illustrated synthesis of the target sample rGO/CS/(Co,Fe)$_x$P$_y$.

Fe)$_x$P$_y$ composite contained phosphorus (P) in addition to the other elements (Fig. 2e and Fig. S7†), with all elements uniformly distributed across the composite. The fine structure of rGO/CS/(Co,Fe)$_x$P$_y$ is further studied by transmission electron microscopy (TEM) (Fig. 2f–h). Low-magnification TEM (Fig. 2f) reveals the sandwich-like structure of rGO/CS, with distinct dark (CS) and bright (rGO) regions. The presence of small nanoparticles on the surface is indicative of the formation of (Co,Fe)$_x$P$_y$, which is further supported by high-magnification TEM images (Fig. 2g). In the enlarged view, these dark nanoparticles are clearly identified as (Co,Fe)$_x$P$_y$. These results confirm the successful synthesis of the rGO/CS/(Co,Fe)$_x$P$_y$ composite. High-resolution TEM (HRTEM) (Fig. 2h) shows lattice fringes corresponding to different crystal planes. A spacing of 0.472 nm was attributed to the (111) plane of CS, while a spacing of 0.281 nm was associated with the (101) plane of Fe$_2$P, and 0.211 nm lattice spacing corresponded to the (201) plane of Co$_2$P. Attributing the different lattice spacings to Co$_2$P and Fe$_2$P requires further validation, as each material typically exhibits distinct lattice parameters. These findings, nonetheless, strongly suggest the multiple interfaces generated for (Co,Fe)$_x$P$_y$ on the rGO/CS structure.

Fig. 3a, b and Fig. S8 (ESI†) depict the XRD patterns of all intermediate and final products synthesized during the preparation of rGO/CS/(Co,Fe)$_x$P$_y$, providing insight into the structural evolution of the composites. The diffraction peaks of rGO/CS correspond well to Co$_2$SiO$_4$ (JCPDS card no. 15-0497) (Fig. 3a).[42] The low intensity of these peaks can be attributed to the silicate's relatively poor crystallinity, as seen in previous studies conducted under hydrothermal conditions. After the *in situ* growth of Co-MOF on rGO/CS, the XRD peaks align with those of pure Co-MOF, though the peak intensity was reduced (Fig. S8†). This is due to the strong crystallinity and numerous diffraction peaks of Co-MOF, which overshadow the weaker and overlapping diffraction peaks of CS.[43] The reduced crystallinity of Co-MOF in the presence of rGO/CS also contributes to the lower peak intensities compared to Co-MOF alone. After the iron ion exchange process, the diffraction peaks of Co-MOF disappear, leaving only the diffraction peaks corresponding to CS (Fig. S8†). This indicates that the Co-MOF has been successfully etched, forming rGO/CS/MOF-derived amorphous Co–Fe compounds (denoted as rGO/CS/Co,Fe-MOF). After the final phosphorization process, the XRD pattern shows diffraction peaks corresponding to both Co$_2$P (JCPDS no. 32-0306) and Fe$_2$P (JCPDS no. 27-1171), in addition to the CS peaks (Fig. 3b). The weak intensities and broad shape of the phosphide peaks suggest a low crystallinity of the (Co,Fe)$_x$P$_y$ phase. This observation is consistent with the unclear phosphide lattice fringes seen in the HRTEM image (Fig. 2h), further supporting the low-crystallinity nature of the synthesized phosphides. Fig. 3c presents the Raman spectra of rGO/CS, (Co,Fe)$_x$P$_y$, rGO/CS/Co$_x$P$_y$, and rGO/CS/(Co,Fe)$_x$P$_y$. All samples exhibit D-peaks at around 1360 cm^{-1} and G-peaks at around 1600 cm^{-1}, characteristic of carbon-based materials.[44] The carbon in (Co,Fe)$_x$P$_y$ arises from the pyrolysis of the Co,Fe-MOF under an inert atmosphere. The intensity ratio of D-peak to G-peak (I_D/I_G) reflects the degree of disorder in the carbon structure, with higher values indicating more amorphous carbon.[45,46] The rGO/CS and rGO/CS/Co$_x$P$_y$ samples, which were not subjected to Fe ion etching, exhibit similar I_D/I_G values of 0.99 and 1.00, respectively. However, after Fe ion etching and doping, the I_D/I_G ratios of rGO/CS/(Co,Fe)$_x$P$_y$ and (Co,Fe)$_x$P$_y$ decrease to 0.90 and 0.91, respectively, suggesting an increase in the ratio of sp^3-hybridized carbon.[47] This may result from the enhanced coordination of carbon within the MOF structure after Fe incorporation, which leads to a

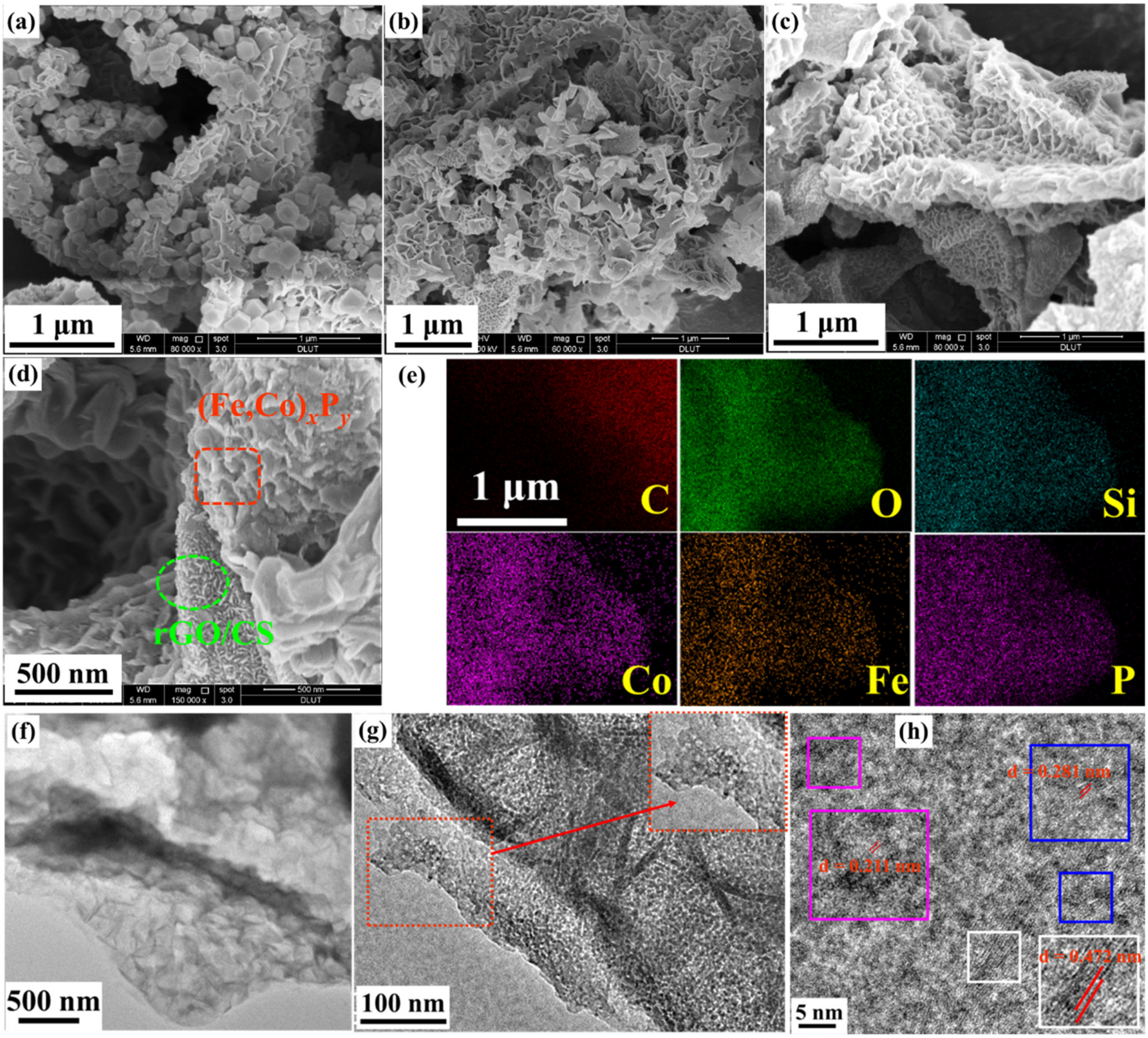

Fig. 2 Morphology of the samples: the SEM images of (a) rGO/CS/Co-MOF, (b) rGO/CS/Co,Fe-MOF, and (c–d) rGO/CS/(Co,Fe)$_x$P$_y$; (e) elemental images of rGO/CS/(Co,Fe)$_x$P$_y$; (f–g) TEM images of rGO/CS/(Co,Fe)$_x$P$_y$, inserting an enlarged image; (h) HRTEM image of rGO/CS/(Co,Fe)$_x$P$_y$, inserting the partial enlargements.

decrease in the degree of structural disorder and improves the electrical conductivity. The bonding information for these composites was further explored using FTIR spectroscopy (Fig. 3d). The peaks at approximately 454 cm^{-1}, 810 cm^{-1}, and 1010 cm^{-1} are attributed to the symmetric stretching vibrations of Si–O bonds, asymmetric stretching vibrations of Si–O bonds, and asymmetric stretching vibrations of Si–O–Si bonds, respectively, originating from the rGO/CS support.[25] Additionally, the Co–O bond in CS is observed around 670 cm^{-1}, and peaks near 1600 cm^{-1} correspond to functional groups in rGO. After the growth of (Co,Fe)$_x$P$_y$ on rGO/CS, the Si–O–Si bond at 1010 cm^{-1} and the Si–O bond at 454 cm^{-1} exhibit a blue shift (toward higher wavenumbers). This shift is caused by spatial constraints from the (Co,Fe)$_x$P$_y$ layers grown on the rGO/CS surface, altering the local chemical environment of these bonds. Moreover, a new peak at around 540 cm^{-1}, corresponding to a P–O bond, appears in the spectrum of rGO/CS/(Co,Fe)$_x$P$_y$.[24] This peak suggests the formation of chemical bonds between phosphorus in the (Co,Fe)$_x$P$_y$ layer and oxygen in the rGO/CS structure. Notably, the P–O peak is absent in the spectrum of (Co,Fe)$_x$P$_y$ alone, further confirming the chemical interaction between the layers. Similarly, the rGO/CS/Co$_x$P$_y$ sample also shows a blue shift in Si–O–Si and Si–O bonds and appearance of a P–O bond, supporting the analyses of the rGO/CS/(Co,Fe)$_x$P$_y$ composite.

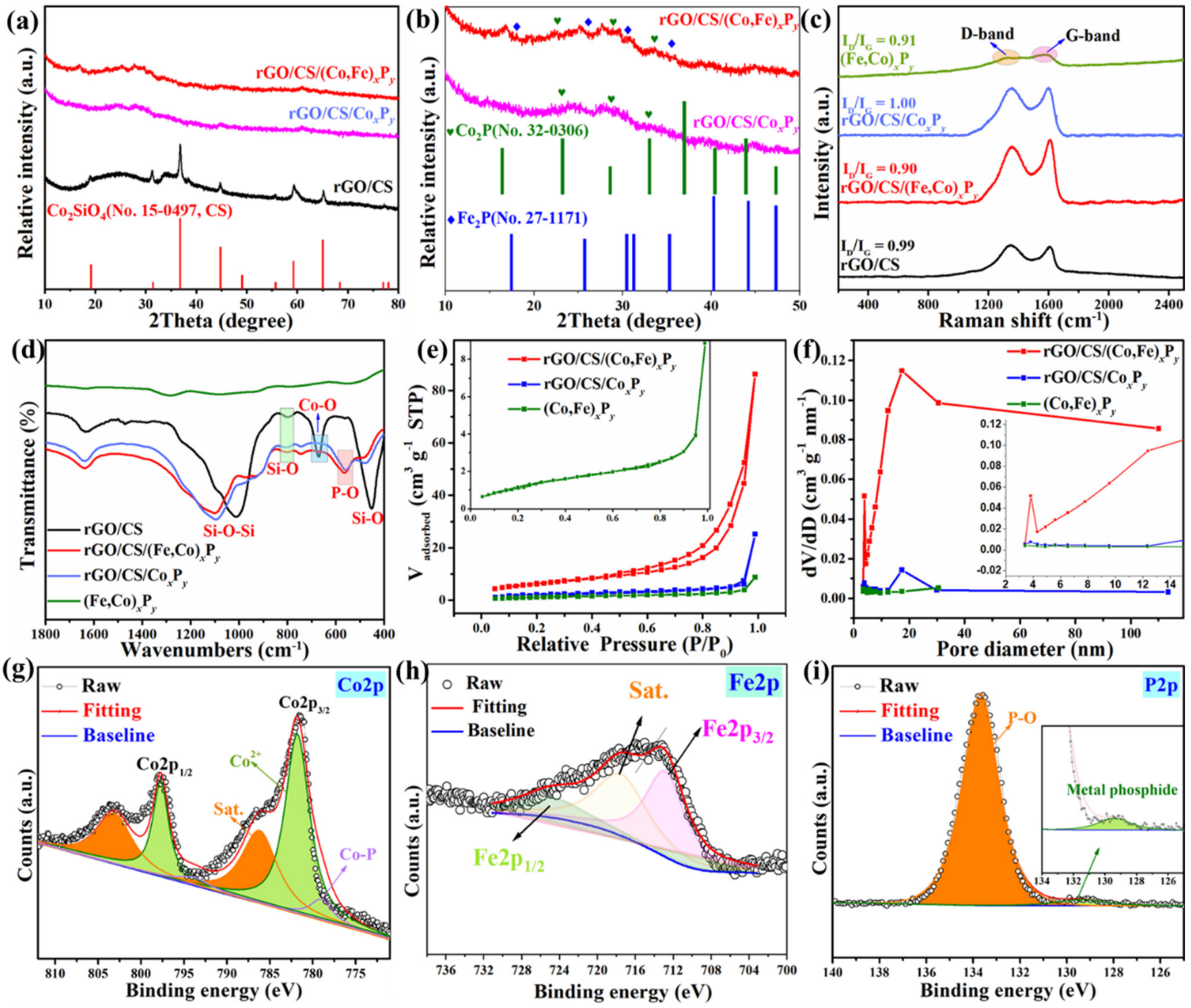

Fig. 3 Composition and structural characterization of the samples: (a and b) XRD patterns of rGO/CS, rGO/CS/Co_xP_y and rGO/CS/$(Co,Fe)_xP_y$; (c) FTIR and (d) Raman spectra of rGO/CS, $(Co,Fe)_xP_y$, rGO/CS/Co_xP_y and rGO/CS/$(Co,Fe)_xP_y$; (e) nitrogen adsorption–desorption isotherms and (f) pore size-distribution curves calculated by the BJH method of $(Co,Fe)_xP_y$, rGO/CS/Co_xP_y and rGO/CS/$(Co,Fe)_xP_y$; (g) Co 2p, (h) Fe 2p and (i) P 2p XPS spectra of rGO/CS/$(Co,Fe)_xP_y$.

The specific surface area and pore size were determined through nitrogen (N_2) adsorption/desorption isotherms, as presented in Fig. 3e and Fig. S9 (ESI†). The rGO/CS sample exhibits a typical type IV isotherm (Fig. S9†), proving mesoporosity, while the $(Co,Fe)_xP_y$ sample presents a typical type II isotherm (Fig. 3e), which is characteristic of macroporous materials. Interestingly, both rGO/CS/Co_xP_y and rGO/CS/$(Co,Fe)_xP_y$ display hybrid isotherms (Fig. 3e), combining features of both types. This indicates the successful integration of the phosphide layer with the rGO/CS structure. The specific surface areas of rGO/CS, $(Co,Fe)_xP_y$, rGO/CS/Co_xP_y, and rGO/CS/$(Co,Fe)_xP_y$ were measured to be 358, 4, 7 and 26 $m^2\ g^{-1}$, respectively. The phosphide layer exhibits a relatively small surface area, while rGO/CS has a much larger one. As observed in the SEM and TEM images (Fig. 2), the phosphide layer partially covers the rGO/CS structure, leading to a significant reduction in surface area.[22] However, despite this decrease, the phosphide layer introduces a variety of active sites that enhance the material's OER performance. Pore size distribution plots obtained through the Barrett–Joyner–Halenda (BJH) method (Fig. 3f and Fig. S10, ESI†) reveal that all four materials feature pores in the range of 3.8 nm, placing them within the mesopore category. In comparison to rGO/CS, the phosphide-containing samples ($(Co,Fe)_xP_y$, rGO/CS/Co_xP_y, and rGO/CS/$(Co,Fe)_xP_y$) display increased pore sizes, measured at 5.6 nm, 7.8 nm, 17.4 nm, and 17.4 nm, respectively. The stacked growth of the phosphide layers on rGO/CS contributes to these enlarged pore sizes, further enhancing the mesoporous and macroporous properties of the composites. These larger pore sizes are favorable for electrocatalytic reactions, as they facilitate efficient diffusion of reactants and products.

To study the elemental composition and chemical states of rGO/CS/$(Co,Fe)_xP_y$, X-ray photoelectron spectroscopy (XPS) was performed (Fig. 3g–i and Fig. S11 in the ESI†). The XPS survey spectrum (Fig. S11a†) confirms the presence of six key elements: carbon (C), oxygen (O), silicon (Si), cobalt (Co), iron (Fe), and phosphorus (P). The C 1s spectrum (Fig. S11b†) reveals multiple carbon environments, including C–C/C═C (284.3 eV), C–O (285.1 eV), and C═O (288.2 eV), which are mainly attributed to rGO. The binding energy at 285.9 eV previously assigned to C═N is more likely related to the carbon framework of the MOF and its derivatives, though its specific assignment requires further validation.[48] The O 1s spectrum (Fig. S11d†) shows three distinct peaks. The first at 533.3 eV assigns to the P–O bond in the $(Co,Fe)_xP_y$ layer, while peaks at 532.3 eV and 531.2 eV are indexed to oxygen vacancies and the Si–O–Co bond within the rGO/CS structure.[49,50] The presence of oxygen vacancies is known to promote electrocatalytic activity by improving charge transfer kinetics.[51] The Si 2p spectrum (Fig. S11c†) displays a prominent peak at 103.0 eV, corresponding to Si in its tetravalent oxidation state, characteristic of silicates.[50] The Co 2p spectrum (Fig. 3g) reveals peaks corresponding to Co $2p_{3/2}$ and Co $2p_{1/2}$, along with their satellite features. The peaks at 778.8 eV and 793.8 eV are attributed to Co–P bonding in the $(Co,Fe)_xP_y$ phase, while the peaks at 781.8 eV and 797.7 eV correspond to Co^{2+} in cobalt silicate and Co_2P.[52] The 15.9 eV separation between these two peaks also confirms the presence of Co^{2+} in both CS and Co_2P.[41] Similarly, the Fe 2p spectrum (Fig. 3h) shows binding energies at 712.4 eV (Fe $2p_{3/2}$) and 724.9 eV (Fe $2p_{1/2}$), with a satellite peak at 717.3 eV, indicative of Fe species in the $(Co,Fe)_xP_y$ phase.[40] The P 2p spectrum (Fig. 3i) displays two peaks: one at 133.6 eV, corresponding to the P–O bond, and another at 129.4 eV, attributed to metal phosphides (Co_2P and Fe_2P).[53] The relatively weak intensity of the metal phosphide peaks is likely due to two factors: the low crystallinity of the $(Co,Fe)_xP_y$ layer, as evidenced by the broad XRD peaks, and possible electronic interactions between Fe_2P and Co_2P, which could weaken the individual phosphide features.[54] To further quantify the elemental composition of rGO/CS/$(Co,Fe)_xP_y$, the results of energy-dispersive X-ray spectroscopy (EDS) and XPS were compared (Table S1†). XPS results show the atomic percentages of 31.5% C, 43.2% O, 5.5% Si, 10.1% P, 6.7% Co, and 3.0% Fe. EDS results show slightly different weight percentages: 34.7% C, 3.72% O, 5.9% Si, 9.4% P, 8.9% Co, and 3.9% Fe. Inductively coupled plasma atomic emission spectroscopy (ICP-AES) confirms the presence of 8.8 wt% P, 7.8 wt% Co, and 3.5 wt% Fe in the sample. The results prove the successful incorporation of Co_2P and Fe_2P into the rGO/CS/$(Co,Fe)_xP_y$ composite, contributing additional active sites for both HER and OER. All of the above characterization methods confirm the successful synthesis of rGO/CS/$(Co,Fe)_xP_y$, which is a promising candidate for OWS electrocatalysis.

To evaluate the catalytic activities of rGO/CS/$(Co,Fe)_xP_y$, both the OER and HER were investigated in 1 M KOH electrolyte using a three-electrode configuration. One of the most important parameters for assessing the electrocatalyst performance is the overpotential (η), which was obtained through linear sweep voltammetry (LSV). First, the chosen rGO/CS support exhibited an η value of 390 mV (10 mA cm^{-2}) (Fig. 4a). Next, the influence of varying Fe content on η of rGO/CS/Co,Fe-MOF was explored. Co-MOF was grown on the rGO/CS's surface, followed by etching with different concentrations of Fe ions, introducing new Co and Fe active sites. The samples, designated as rGO/CS/Co,Fe-MOF-1, rGO/CS/Co,Fe-MOF-2, and rGO/CS/Co,Fe-MOF-3, correspond to the use of 5, 9, and 13 mg of $FeSO_4 \cdot 7H_2O$, respectively. All samples showed a reduction in η compared to the rGO/CS carrier (Fig. S12a, ESI†), indicating improved OER activity. Among these, rGO/CS/Co,Fe-MOF-2 demonstrated the lowest η value of 340 mV at 10 mA cm^{-2} and was selected for further processing. This sample is referred to as rGO/CS/Co,Fe-MOF in the subsequent discussion. The next step involved the phosphorization of rGO/CS/Co,Fe-MOF using different quantities of a phosphorus source. The resulting rGO/CS/$(Co,Fe)_xP_y$ samples were named rGO/CS/$(Co,Fe)_xP_y$-1, rGO/CS/$(Co,Fe)_xP_y$-2, and rGO/CS/$(Co,Fe)_xP_y$-3 based on the use of 100, 500, and 1000 mg of $NaH_2PO_2 \cdot H_2O$, respectively. As shown in Fig. S12b,† all samples exhibited significant enhancement in OER activity, and η values were 330 mV, 256 mV, and 280 mV (10 mA cm^{-2}), respectively. Thus, rGO/CS/$(Co,Fe)_xP_y$-2, with an η of 256 mV at 10 mA cm^{-2}, showed the best OER activity and was chosen as the target sample, hereafter referred to as rGO/CS/$(Co,Fe)_xP_y$ unless otherwise specified. To further highlight the superior performance of rGO/CS/$(Co,Fe)_xP_y$, comparisons were made with samples synthesized without iron etching (rGO/CS/Co_xP_y) and without the rGO/CS carrier ($(Co,Fe)_xP_y$), following the same preparation method (details in the ESI†). Fig. 4a summarizes the LSV curves of various samples: rGO/CS, rGO/CS/Co,Fe-MOF, rGO/CS/$(Co,Fe)_xP_y$, rGO/CS/Co_xP_y, and $(Co,Fe)_xP_y$. The OER performance follows the trend: rGO/CS/$(Co,Fe)_xP_y$ > rGO/CS/Co_xP_y > $(Co,Fe)_xP_y$ > rGO/CS/Co,Fe-MOF > rGO/CS. The respective η values (10 mA cm^{-2}) are 390 mV, 340 mV, 256 mV, 304 mV, and 317 mV. As illustrated in Fig. 4b and summarized in Table S2,† the η value of rGO/CS/$(Co,Fe)_xP_y$ is superior to most reported OER electrocatalysts based on transition metal silicates (TMSs) and other transition metal materials. In particular, the η of 256 mV (10 mA cm^{-2}) is much lower than that of Co nanoparticles@N-doped carbon on rGO/CS (278 mV)[25] and CoP nanoparticles on cobalt silicate (309 mV).[24] These results demonstrate that the integration of $(Co,Fe)_xP_y$ on the rGO/CS support can substantially improve the OER performance of cobalt silicates, showcasing the superiority of this synthesis strategy compared to other cobalt silicate-based materials. Moreover, the OER performance of rGO/CS/$(Co,Fe)_xP_y$ is slightly better than that of commercially available RuO_2 (260 mV at 10 mA cm^{-2}), as depicted in Fig. 4b and Fig. S13 (ESI†). In practical applications, the η value at high current densities is a crucial parameter. As depicted in Fig. S13,† at

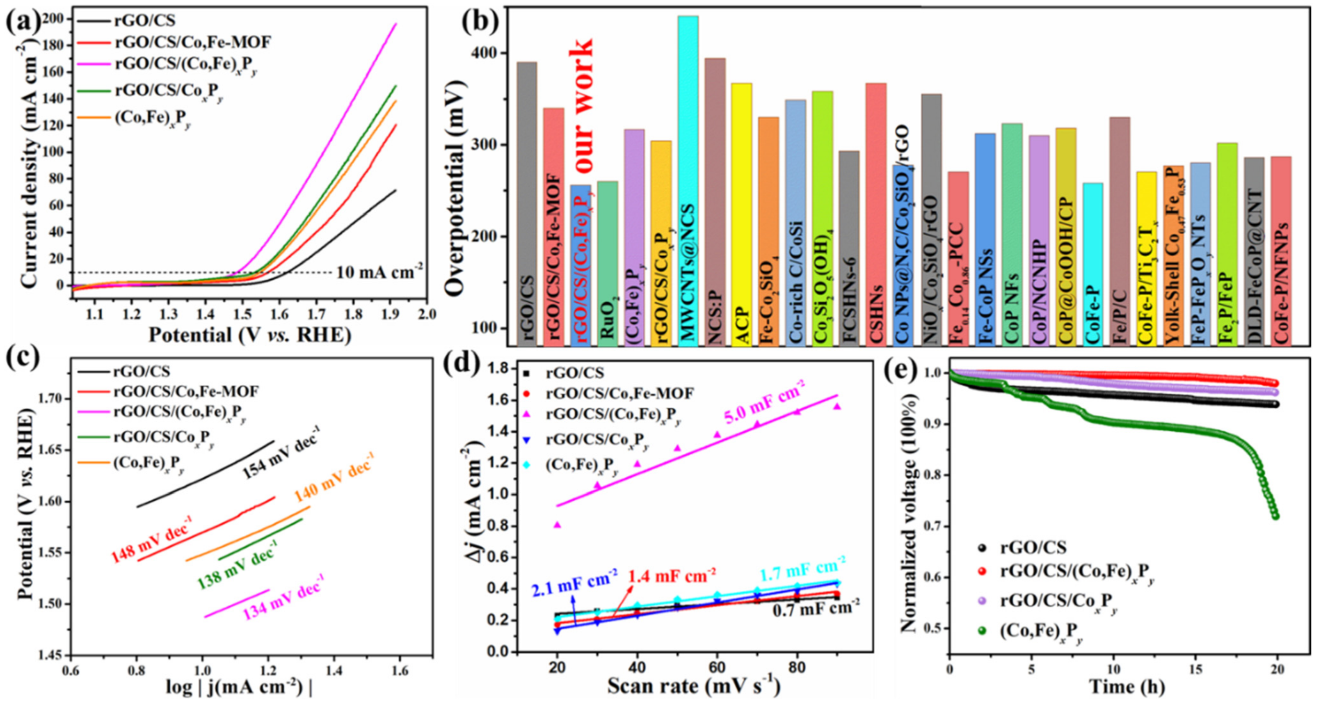

Fig. 4 OER properties: (a) LSV curves of rGO/CS, rGO/CS/Co,Fe-MOF, rGO/CS/(Co,Fe)$_x$P$_y$, rGO/CS/Co$_x$P$_y$ and (Co,Fe)$_x$P$_y$; (b) overpotentials achieved in this work compared with the reported TMSs and some Co-based materials at 10 mA cm^{-2}; (c) the corresponding Tafel plots of rGO/CS, rGO/CS/Co,Fe-MOF, rGO/CS/(Co,Fe)$_x$P$_y$, rGO/CS/Co$_x$P$_y$ and (Co,Fe)$_x$P$_y$; (d) linear relationships of capacitive current *vs.* scan rate of rGO/CS, rGO/CS/Co,Fe-MOF, rGO/CS/(Co,Fe)$_x$P$_y$, rGO/CS/Co$_x$P$_y$ and (Co,Fe)$_x$P$_y$; (e) the voltage stable performance of rGO/CS, rGO/CS/(Co,Fe)$_x$P$_y$, rGO/CS/Co$_x$P$_y$ and (Co,Fe)$_x$P$_y$ tested at 10 mA cm^{-2} (voltage normalization).

current densities above 20 mA cm^{-2}, the catalytic activity of rGO/CS/(Co,Fe)$_x$P$_y$ significantly surpasses that of RuO$_2$.[20] For instance, at 100 mA cm^{-2}, rGO/CS/(Co,Fe)$_x$P$_y$ exhibits an η value of only 488 mV, which is substantially lower than that of RuO$_2$ (645 mV), further underscoring its high catalytic activity. The exceptional OER performance of the target sample rGO/CS/(Co,Fe)$_x$P$_y$ can be attributed to several factors: first, the incorporation of a small amount of Fe introduces additional active sites.[55] Second, both the metal phosphide and the silicate/rGO support possess inherent OER activity, and the two components work synergistically to enhance the performance.[56] Third, the amorphous structure of rGO/CS/(Co,Fe)$_x$P$_y$ (Fig. 3a and b) provides unique electronic configurations and the presence of vacancies (Fig. S11d†), which promote the formation of active sites and facilitate mass transfer.[57]

The Tafel slope (*b*) is a crucial kinetic parameter for evaluating OER electrocatalysts, with lower values indicating more favorable OER kinetics.[58] Fig. 4c shows the Tafel plots of rGO/CS, rGO/CS/Co,Fe-MOF, rGO/CS/(Co,Fe)$_x$P$_y$, rGO/CS/Co$_x$P$_y$, and (Co,Fe)$_x$P$_y$, providing insight into their OER kinetics. Among all samples, rGO/CS/(Co,Fe)$_x$P$_y$ exhibits the smallest *b* value of 134 mV dec^{-1}, demonstrating the fastest OER kinetics. This superior performance is attributed to excellent mass transfer capabilities enabled by the material's unique, carefully designed structure. The Tafel slope of approximately 120 mV dec^{-1} for rGO/CS/(Co,Fe)$_x$P$_y$ suggests that the rate-determining step involves conversion of HO* intermediate to *O intermediates.[59] Based on the Tafel slope values (rGO/CS/(Co,Fe)$_x$P$_y$ < rGO/CS/Co$_x$P$_y$ < (Co,Fe)$_x$P$_y$ < rGO/CS/Co,Fe-MOF < rGO/CS), it can be inferred that the presence of metal phosphides accelerates the OER kinetics.

To explore the intrinsic activity of the electrocatalysts, cyclic voltammetry (CV) measurements (Fig. S14, ESI†) were conducted to analyze the double-layer capacitance (C_{dl}), proportional to the electrochemically active surface area (ECSA).[25] A larger ECSA corresponds to a higher number of active sites, facilitating an enhanced interaction with the electrolyte and improved water molecule adsorption.[60] In Fig. 4d and Fig. S15 (ESI†), the C_{dl} values of the samples are as follows: rGO/CS/(Co,Fe)$_x$P$_y$ (5.0 mF cm^{-2}) > rGO/CS/Co$_x$P$_y$ (2.1 mF cm^{-2}) > (Co,Fe)$_x$P$_y$ (1.7 mF cm^{-2}) > rGO/CS/Co,Fe-MOF (1.4 mF cm^{-2}) > rGO/CS (0.7 mF cm^{-2}). This ranking of ECSA-based OER activity is consistent with the earlier electrochemical data, confirming that rGO/CS/(Co,Fe)$_x$P$_y$ exhibits the highest OER performance. The superior C_{dl} value of rGO/CS/(Co,Fe)$_x$P$_y$ can be attributed to its complex 2D double-sandwich-like architecture and the introduction of numerous active sites, further supporting its exceptional OER activity.

Long-term stability is another critical parameter for evaluating OER electrocatalysts. Fig. 4e shows the voltage *vs.* time curves for rGO/CS, rGO/CS/(Co,Fe)$_x$P$_y$, and rGO/CS/Co$_x$P$_y$ (Co,Fe)$_x$P$_y$ measured at 10 mA cm^{-2}. Among these samples, rGO/CS/(Co,Fe)$_x$P$_y$ demonstrates the best durability, retaining 98% of its initial OER activity after 20 hours of continuous testing.

In comparison, the OER activities of rGO/CS, rGO/CS/Co_xP_y and $(Co,Fe)_xP_y$ decrease to 94%, 96%, and 72% of their initial activities, respectively, over the same time period. The poorer stability of the standalone $(Co,Fe)_xP_y$ layer suggests that the rGO/CS support significantly enhances the overall stability of the composite. This improvement is owing to the incorporation of Fe and the formation of the phosphide layer not only increases the number of active sites for OER, but also contributes slightly to improved stability. When combined with the rGO/CS carrier, the stability ranking follows the order: rGO/CS/$(Co,Fe)_xP_y$ > rGO/CS/Co_xP_y > rGO/CS. This enhanced stability is not only due to the strong electronic interactions between the rGO/CS carrier and the $(Co,Fe)_xP_y$ nanoparticles, but also due to the protection of $(Co,Fe)_xP_y$ nanoparticles for CS. To confirm the structural stability of rGO/CS/$(Co,Fe)_xP_y$ after long-term OER testing, SEM was used to characterize the material's morphology (Fig. S16, ESI†). The results show that the lamellar structure of rGO/CS/$(Co,Fe)_xP_y$ remains largely unchanged after testing, with the rGO/CS support maintaining its integrity. The structural features are well-preserved, indicating that the composite possesses excellent stability, which is beneficial for sustained OER performance.

Following the OER tests, the HER activities of rGO/CS/$(Co,Fe)_xP_y$ and comparative samples were measured in 1 M KOH electrolyte. Similar to OER investigation, the influence of Fe content and phosphorization conditions on HER performance was explored. Fig. S17a (ESI†) shows the LSV curves for rGO/CS/Co,Fe-MOF-1, rGO/CS/Co,Fe-MOF-2, and rGO/CS/Co,Fe-MOF-3. Their corresponding η values were measured at 473 mV, 445 mV, and 496 mV *vs.* RHE at 10 mA cm^{-2}, respectively. Among these, rGO/CS/Co,Fe-MOF-2 (represented hereafter as rGO/CS/Co,Fe-MOF) displayed the best HER performance, similar trends with the OER results. Fig. S17b† depicts the LSV curves of rGO/CS, rGO/CS/$(Co,Fe)_xP_y$-1, rGO/CS/$(Co,Fe)_xP_y$-2 and rGO/CS/$(Co,Fe)_xP_y$-3, with the corresponding η values of 607 mV, 360 mV, 180 mV, and 200 mV *vs.* RHE at 10 mA cm^{-2}. The results show that phosphorization significantly enhances the HER activity of the samples. Specifically, rGO/CS/$(Co,Fe)_xP_y$-2 (hereafter referred to as rGO/CS/$(Co,Fe)_xP_y$) achieved the best HER performance, consistent with the OER outcomes. Both the HER and OER results demonstrate that the phosphorization strategy greatly improves the catalytic performance of rGO/CS.

The LSV curves and η values for HER without *iR* compensation for rGO/CS, rGO/CS/Co,Fe-MOF, rGO/CS/$(Co,Fe)_xP_y$, rGO/CS/Co_xP_y and $(Co,Fe)_xP_y$ are presented in Fig. 5a and b. The HER performance follows the trend: rGO/CS/$(Co,Fe)_xP_y$ > rGO/CS/Co_xP_y > $(Co,Fe)_xP_y$ > rGO/CS/Co,Fe-MOF > rGO/CS. The corresponding η values at 10 mA cm^{-2} are 607 mV, 445 mV, 180 mV, 229 mV and 252 mV *vs.* RHE, respectively. These results indicate that HER behavior is primarily driven by the presence of metal phosphides. The introduction of Fe into rGO/CS/Co_xP_y enhances the catalytic performance, confirming that a small amount of Fe can significantly boost activity. In Fig. 5b and Table S3,† the η value of rGO/CS/$(Co,Fe)_xP_y$ is superior to most reported HER electrocatalysts based on TMSs and non-noble metal oxide/hydroxide materials. The η value of 180 mV *vs.* RHE at 10 mA cm^{-2} for rGO/CS/$(Co,Fe)_xP_y$ is notably lower than that of CoP nanoparticles on $Co_3(Si_2O_5)_2(OH)_4$ nanosheets (251 mV *vs.* RHE at 10 mA cm^{-2}).[24] Impressively, the HER activity of rGO/CS/$(Co,Fe)_xP_y$ is even comparable to commercial Pt/C. These comparisons demonstrate that the $(Co,Fe)_xP_y$ on the rGO/CS support can significantly enhance both HER and OER performances in cobalt silicate-based systems.

Similar to the OER, the Tafel slope (*b*) is a critical parameter for analyzing HER kinetics. In alkaline media, the HER process involves two elementary steps: the Volmer reaction ($H_2O + e^- \leftrightarrow {}^*H + OH^-$), which produces adsorbed hydrogen, and either the Heyrovsky reaction (${}^*H + H_2O + e^- \leftrightarrow H_2 + OH^-$) or the Tafel reaction (${}^*H + {}^*H \leftrightarrow H_2$). Tafel slopes of 120, 40, and 30 mV dec^{-1} correspond to Volmer, Heyrovsky, and Tafel steps, respectively.[61] Fig. 5c shows the Tafel slopes of rGO/CS, rGO/CS/Co,Fe-MOF, rGO/CS/$(Co,Fe)_xP_y$, rGO/CS/Co_xP_y and $(Co,Fe)_xP_y$, with the following order: rGO/CS/$(Co,Fe)_xP_y$ < rGO/CS/Co_xP_y < $(Co,Fe)_xP_y$ < rGO/CS/Co,Fe-MOF < rGO/CS. Tafel slopes are 120, 124, 130, 137, and 240 mV dec^{-1}, respectively, indicating that all catalysts follow the Volmer mechanism. The trend confirms that phosphides significantly enhance the adsorption and conversion of reactants during the HER and that the phosphorization process accelerates kinetics. Additionally, the introduction of Fe further improves the reaction kinetics. The synergistic effects of $(Co,Fe)_xP_y$ nanoparticles and the layered structure of rGO/CS result in fast HER kinetics for rGO/CS/$(Co,Fe)_xP_y$.

Fig. S18 (ESI†) presents the CV curves of rGO/CS, rGO/CS/Co,Fe-MOF, rGO/CS/$(Co,Fe)_xP_y$, rGO/CS/Co_xP_y and $(Co,Fe)_xP_y$, while Fig. 5d summarizes their corresponding C_{dl} values, used to estimate the ECSA. The C_{dl} values are ranked as: rGO/CS/$(Co,Fe)_xP_y$ (0.83 mF cm^{-2}) > rGO/CS/Co_xP_y (0.74 mF cm^{-2}) > $(Co,Fe)_xP_y$ (0.51 mF cm^{-2}) > rGO/CS/Co,Fe-MOF (0.38 mF cm^{-2}) > rGO/CS (0.26 mF cm^{-2}). These values align with the OER and HER performances, confirming that rGO/CS/$(Co,Fe)_xP_y$ exhibits the best catalytic activity. Fig. 5e shows the normalized voltage *vs.* time curves for HER stability, measured at −10 mA cm^{-2}. After 20 hours, rGO/CS, rGO/CS/$(Co,Fe)_xP_y$ retains 99% of its initial activity, while rGO/CS, rGO/CS/Co_xP_y and $(Co,Fe)_xP_y$ retain 95%, 96%, and 94%, respectively. The 99% retention in rGO/CS/$(Co,Fe)_xP_y$ demonstrates the synergistic effect between $(Co,Fe)_xP_y$ nanoparticles and the rGO/CS support, further enhancing the HER stability.

The kinetics and interfacial charge transfer processes for both the OER and HER were examined using Nyquist plots (Fig. S19, ESI†). In the high-frequency region, the phosphides reduce the charge-transfer resistance of rGO/CS, indicating excellent electron transport in rGO/CS/$(Co,Fe)_xP_y$. In the low-frequency region, rGO/CS/$(Co,Fe)_xP_y$ exhibits the fastest interfacial electron/mass transfer kinetics owing to its highest slope. These findings support the enhanced HER and OER performances, consistent with the Tafel slope results. The synergistic interaction between the rGO/CS support and $(Co,Fe)_xP_y$ nanoparticles maximizes the adsorption and conversion

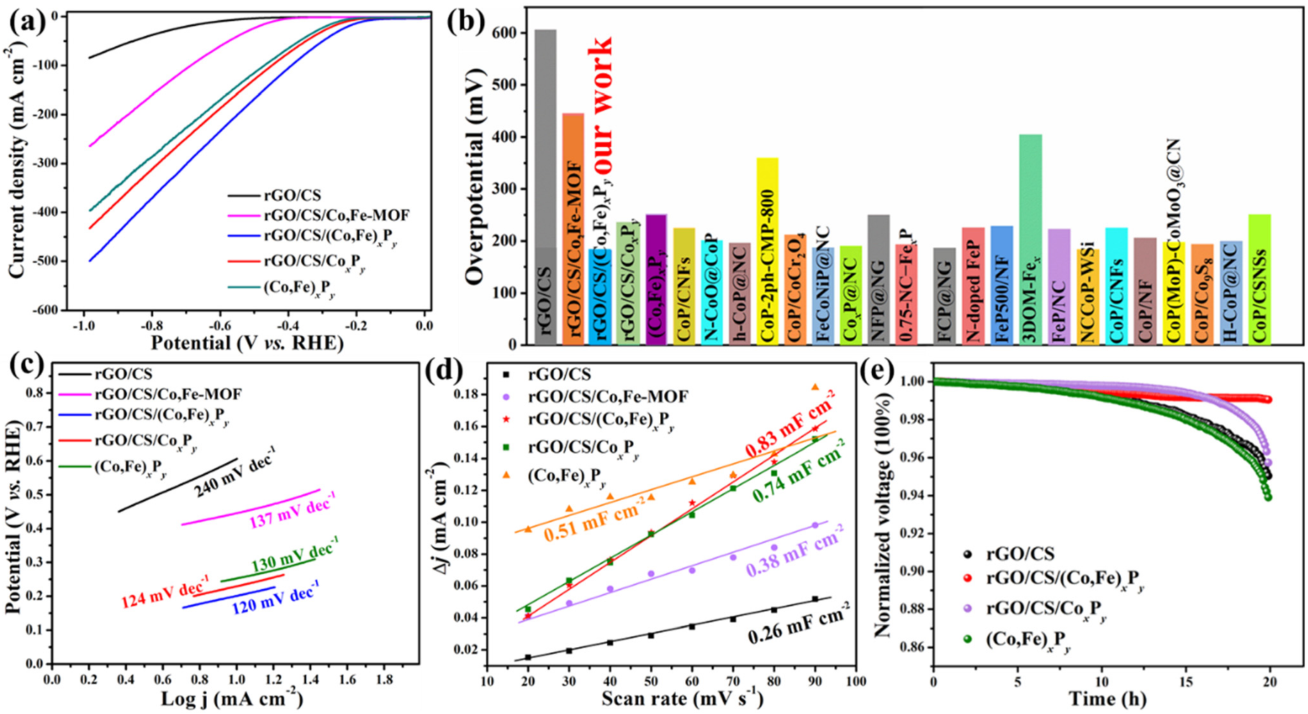

Fig. 5 HER properties: (a) LSV curves of rGO/CS, rGO/CS/Co,Fe-MOF, rGO/CS/(Co,Fe)$_x$P$_y$, rGO/CS/Co$_x$P$_y$ and (Co,Fe)$_x$P$_y$; (b) compared overpotentials; (c) the corresponding Tafel plots of rGO/CS, rGO/CS/Co,Fe-MOF, rGO/CS/(Co,Fe)$_x$P$_y$, rGO/CS/Co$_x$P$_y$ and (Co,Fe)$_x$P$_y$; (d) linear relationships of capacitive current *vs.* scan rate of rGO/CS, rGO/CS/Co,Fe-MOF, rGO/CS/(Co,Fe)$_x$P$_y$, rGO/CS/Co$_x$P$_y$ and (Co,Fe)$_x$P$_y$; (e) the voltage stable performance of rGO/CS, rGO/CS/(Co,Fe)$_x$P$_y$, rGO/CS/Co$_x$P$_y$ and (Co,Fe)$_x$P$_y$ tested at 10 mA cm^{-2} (voltage normalization).

of water and OH$^-$, suggesting that rGO/CS/(Co,Fe)$_x$P$_y$ is an excellent candidate for OWS.[62]

In light of the remarkable OER and HER performances, a two-electrode electrolyzer was assembled using rGO/CS/(Co,Fe)$_x$P$_y$ as both the cathode and anode for OWS. Initially, the current density of the rGO/CS/(Co,Fe)$_x$P$_y$ (+/−) system appears modest (Fig. 6a). The onset of water splitting is primarily dictated by thermodynamic processes, with kinetic effects becoming more pronounced as the applied voltage increases.[63] Notably, the rGO/CS/(Co,Fe)$_x$P$_y$ (+/−) system requires a low cell voltage of 1.41 V to 10 mA cm^{-2}, outperforming the Pt/C(−)||RuO$_2$(+) cell, which requires 1.56 V. This is particularly significant, as the typical range for Pt/C(−)||RuO$_2$(+) cell voltages is reported between 1.50 V and 1.62 V in the literature,[24] demonstrating that the rGO/CS/(Co,Fe)$_x$P$_y$ system is effectively optimized. The superior performance of the rGO/CS/(Co,Fe)$_x$P$_y$ system can be attributed to its distinctive sandwich-like structure, where the mutual synergy between (Co,Fe)$_x$P$_y$ and rGO/CS two-component active sites plays a critical role, especially at higher potentials. The proximity of (Co,Fe)$_x$P$_y$ and rGO/CS facilitates the dissociation of H$_2$O and the adsorption of OH$^-$ ions in alkaline electrolytes, thereby enhancing the catalytic activity. This is particularly evident in the enhanced performance of rGO/CS/(Co,Fe)$_x$P$_y$ in the two-electrode system for OWS, compared to its performance in the three-electrode setup. For example, while the combined HER and OER half-reactions predict a potential difference of 1.66 V (10 mA cm^{-2}), the actual cell voltage required by the rGO/CS/(Co,Fe)$_x$P$_y$ system is only 1.41 V, a potential candidate for efficient water splitting. The stability of the rGO/CS/(Co,Fe)$_x$P$_y$ catalyst is further confirmed by the LSV curves obtained before and after durability testing, which show no significant changes (Fig. 6b), demonstrating the exceptional durability of the catalyst.

Based on the superior catalytic data, several factors may contribute to the outstanding performance of rGO/CS/(Co,Fe)$_x$P$_y$ in the OER and HER in OWS (Fig. 6c): (1) a double-sandwiched structure induced inner-electric field: the rGO/CS/(Co,Fe)$_x$P$_y$ catalyst features a double-sandwich structure, with rGO nanosheets as the inner layer, CS in the middle, and (Co,Fe)$_x$P$_y$ nanoparticles on the outer layer. The inner-electric field generated by the (Co,Fe)$_x$P$_y$ and rGO ensures efficient electron and ion transport.[64] (2) The synergistic effect between CS, rGO, and (Co,Fe)$_x$P$_y$: the surface nature of the (Co,Fe)$_x$P$_y$ nanoparticles introduces a greater number of active sites, thereby in the process of dissociation (H–OH bonds) and the adsorption (OH$^-$ reactants) the interfacial electron transfer kinetics is improved.[24] Besides, it provides protection to the CS and prolongs the catalytic stability. In conclusion, the rGO/CS/(Co,Fe)$_x$P$_y$ system demonstrates an outstanding balance of structure, conductivity, and catalytic activity, making it a promising candidate for efficient and durable OWS applications.

To further understand the superior catalytic performance of rGO/CS/(Co,Fe)$_x$P$_y$ in OWS, the interaction between CS and (Co,Fe)$_x$P$_y$ at the molecular level was investigated using density

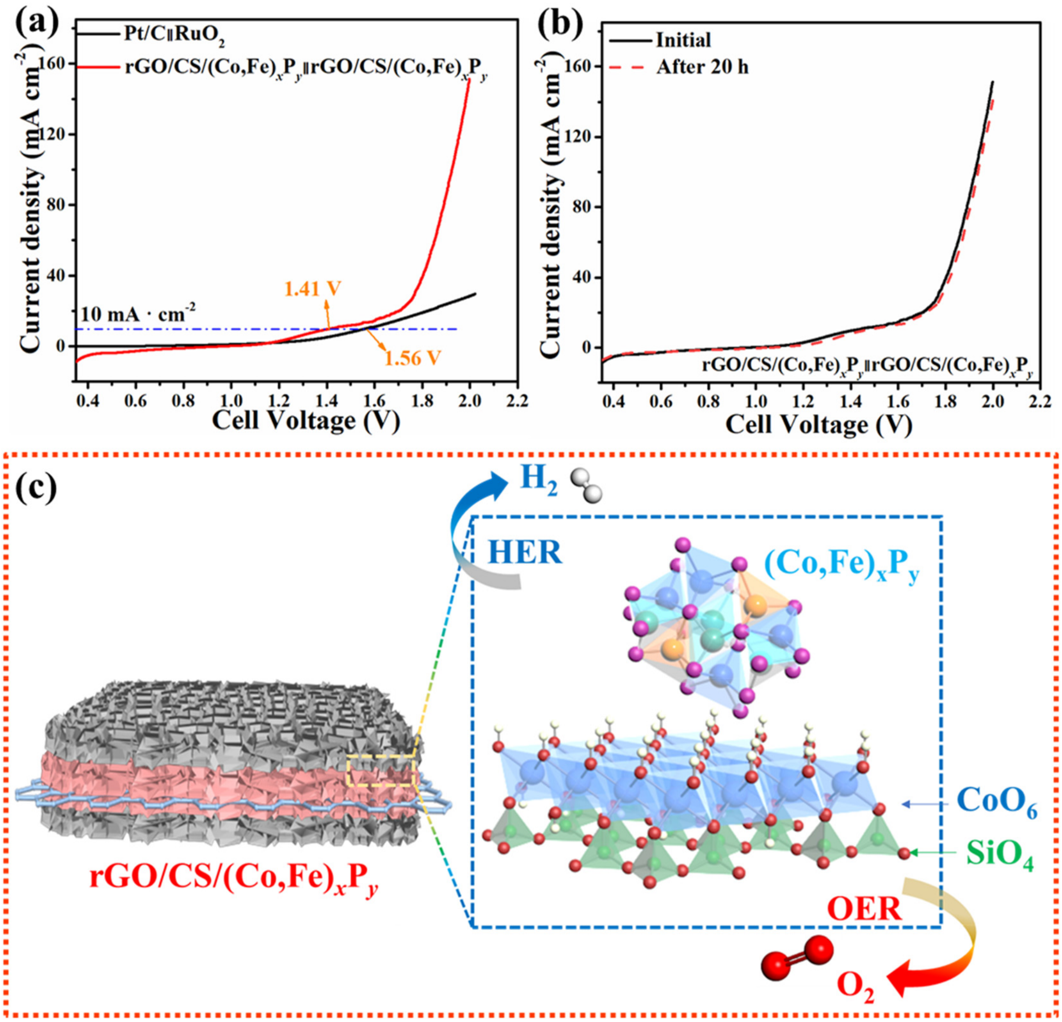

Fig. 6 (a) LSV curves of the two-electrode configuration in 1 M KOH: rGO/CS/(Co,Fe)$_x$P$_y$ (+/−) and 20 wt% Pt/C$^{(-)}$||RuO$_2$$^{(+)}$ benchmark. (b) LSV curves of rGO/CS/(Co,Fe)$_x$P$_y$ (+/−) before and after 20 h chronopotentiometry measurements in 1 M KOH. (c) Graphical illustration of rGO/CS/(Co,Fe)$_x$P$_y$ for simultaneously boosting OER and HER processes by the adjacent dual-active centers.

functional theory (DFT) calculations. To simulate this system effectively, three structures were modeled: pure CS, Co_2P on CS (denoted as CS-CP), and Fe_2P on CS (CS-FP). Band structures, electron density differences and density of states (DOS) are calculated using the crystal structures of CS (Fig. S20a and b, ESI†), CS-CP (Fig. 7a and b), and CS-FP (Fig. 7d and e). The band structures of CS, CS-CP, and CS-FP are shown in Fig. S20c,† Fig. 7c, and f, respectively. The results indicate a decrease in the bandgap from CS to CS-CP and CS-FP, with CS-FP exhibiting the smallest bandgap. This reduction in bandgap demonstrates that CS' conductivity is significantly enhanced by Co_2P and Fe_2P. Furthermore, the convex nature of the energy bands in the CS-CP and CS-FP structures suggests a strong built-in electric field generated between CS and the phosphides.[65] The increased carrier effective mass further indicates improved conductivity in CS-CP and CS-FP, confirming that the introduction of (Co,Fe)$_x$P$_y$ nanoparticles on CS reduces the electron transport barrier and generates a built-in electric field for CS, thereby accelerating the reaction kinetics and enhancing the OWS performance.[66] Fig. S21a–d (ESI†) compare the full DOS of CS, CS-CP, and CS-FP. In CS-CP and CS-FP, the weakening of localized spikes indicates that electrons are more delocalized and more easily bonded, contributing to better conductivity. Fig. S21e† shows PDOS curves for the Co 3d orbitals in CS, CS-CP, and CS-FP. In the CS-CP and CS-FP structures, the Co 3d band center is elevated, and the M–O antibonding orbitals (σ*) are weakened, resulting in stronger bonding. This stronger bonding helps stabilize the intermediates involved in the rate-determining steps of the OWS reaction.[67] The electron density difference (EDD) maps for CS, CS-CP, and CS-FP (Fig. 7g–i) show the redistribution of the electron density. Blue regions indicate electron loss, while red regions represent electron gain. In the CS-CP and CS-FP structures, the blue regions become more prominent, indicating a decrease in electron cloud density, which is favorable for the adsorption of OH^- ions. Interestingly, Fe_2P exerts a stronger influence on cobalt in cobalt silicate when compared to Co_2P. Additionally, the closer the

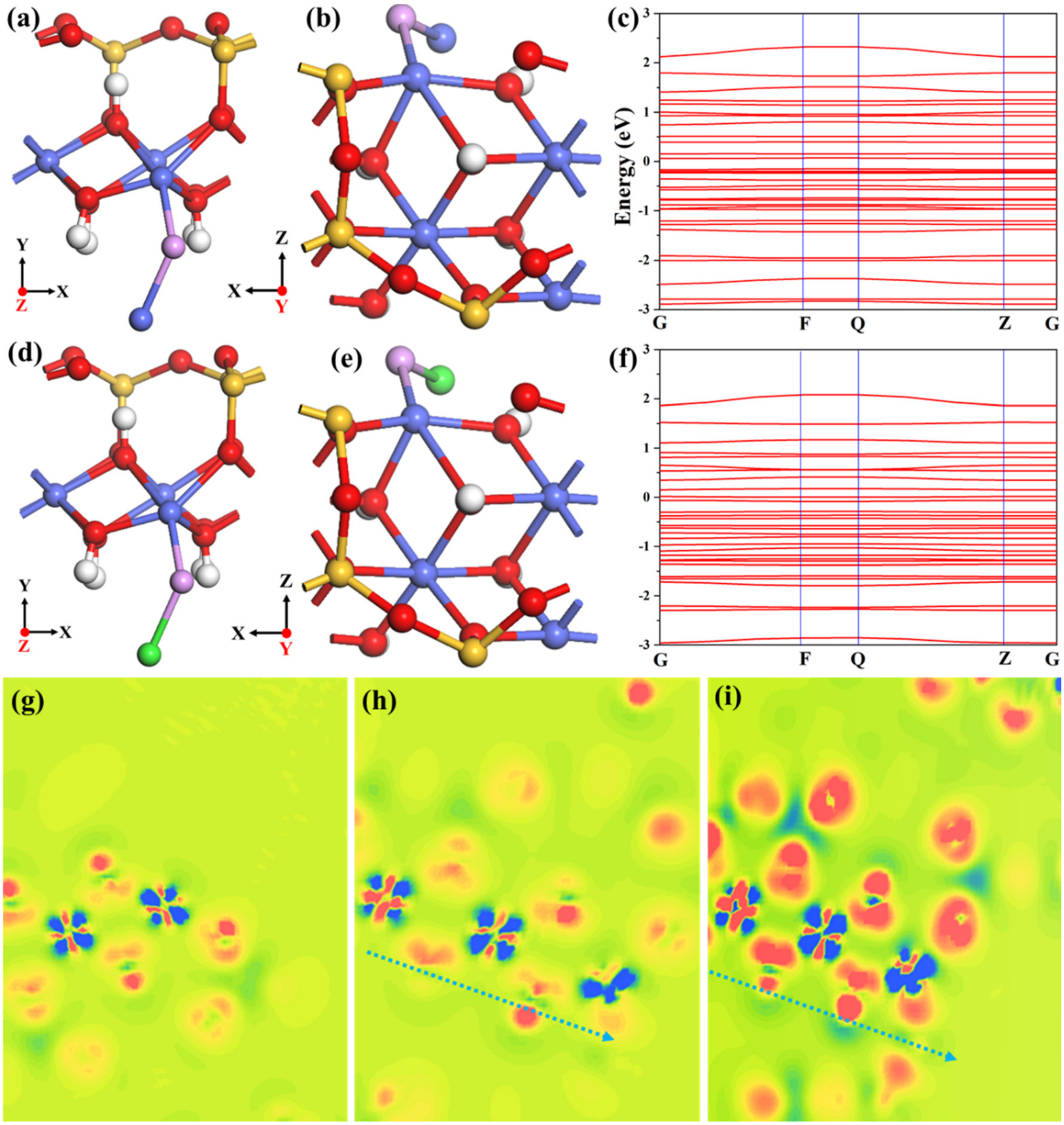

Fig. 7 DFT calculations: crystal structures at different views (a–b) and the band structure (c) of CS-CP; crystal structures at different views (d–e) and the band structure (f) of CS-FP; (g–i) EDD of CS, CS-CP and CS-FP.

cobalt atoms are to phosphorus atoms, the lower their charge density, further enhancing their catalytic activity. The DFT calculations clearly demonstrate that the introduction of $(Co,Fe)_xP_y$ nanoparticles on CS induced a built-in electric field and improves the overall conductivity, as well as facilitates fast reaction kinetics. This synergistic interaction is key to the enhanced OWS properties of rGO/CS/$(Co,Fe)_xP_y$.

3. Conclusion

In summary, a double-sandwich rGO/CS/$(Co,Fe)_xP_y$ architecture constituted of CS, rGO, and $(Co,Fe)_xP_y$ was designed and successfully synthesized that served as an exceptional bifunctional electrocatalyst for OWS. Both experimental results and DFT calculations confirm the synergistic interaction between CS, $(Co,Fe)_xP_y$, and the rGO scaffold, which enhances the conductivity and accelerates reaction kinetics by improving H–OH bond dissociation and OH^- adsorption. Moreover, the built-in electric field generated at the multiple interfaces further boosts charge transfer, contributing to the catalyst's exceptional performance in OWS. The rGO/CS/$(Co,Fe)_xP_y$ catalyst achieves low overpotentials of 256 mV for OER and 180 mV for HER at 10 mA cm^{-2}, surpassing most reported electrocatalysts based on TMSs and even rivaling commercial RuO_2 and Pt/C. Additionally, the rGO/CS/$(Co,Fe)_xP_y$ (+/−) system requires just

1.41 V for OWS at 10 mA cm^{-2}, outperforming many recently developed bifunctional electrocatalysts and the commercial Pt/C||RuO_2 system. This outstanding catalytic performance is owing to the well-designed structure, the introduction of new active sites from the rGO and $(Co,Fe)_xP_y$ layers, and the built-in electric field that enhances interfacial electron transfer kinetics. This study not only demonstrates the effectiveness of incorporating $(Co,Fe)_xP_y$ active sites into the rGO/CS support for superior OER, HER, and OWS performance, but also provides a promising strategy for the surface engineering of Earth-abundant, non-noble metal bifunctional electrocatalysts for clean energy conversion.

Data availability

The data supporting this article have been included as part of the ESI.†

Conflicts of interest

There are no conflicts to declare.

Acknowledgements

We thank the Doctoral Research Start-up Fund of Hubei University of Science and Technology (BK202504) and the Natural Science Foundation of Liaoning Province (2023-MS-115) for supporting this work. We also thank the National Natural Science Foundation of China (22305028) and the Dalian Minzu University Doctoral Program (120164) for supporting this work.

References

1 I. Slobodkin, E. Davydova, M. Sananis, A. Breytus and A. Rothschild, Electrochemical and chemical cycle for high-efficiency decoupled water splitting in a near-neutral electrolyte, *Nat. Mater.*, 2024, **23**, 398–405.

2 X. Chen, X. Li, Y. Peng, H. Yang, Y. Tong, M.-S. Balogun and Y. Huang, Tailoring Carrier Dynamics of $BiVO_4$ Photoanode via Dual Incorporation of Au and $Co(OH)_x$ Cooperative Modification for Photoelectrochemical Water Splitting, *Adv. Funct. Mater.*, 2024, 2416091, DOI: 10.1002/adfm.202416091.

3 Y. Wang, D. Chen, J. Zhang, M.-S. Balogun, P. Wang, Y. Tong and Y. Huang, Charge Relays via Dual Carbon-Actions on Nanostructured $BiVO_4$ for High Performance Photoelectrochemical Water Splitting, *Adv. Funct. Mater.*, 2022, **32**, 2112738.

4 Y. Wang, Y. Chen, Y. Yun, X. Hong, Y. Huang and H. Ji, CoMoP hole transfer layer functionally enhances efficiency and stability of $BiVO_4$ based photoanode for solar water splitting, *Appl. Catal., B*, 2024, **358**, 124375.

5 Y. Wang, L. Li, S. Wang, X. Dong, C. Ding, Y. Mu, M. Cui, T. Hu, C. Meng and Y. Zhang, Anion Structure Regulation of Cobalt Silicate Hydroxide Endowing Boosted Oxygen Evolution Reaction, *Small*, 2024, **20**, 2401394.

6 H. G. Xu, X. Y. Zhang, Y. Ding, H. Q. Fu, R. Wang, F. Mao, P. F. Liu and H. G. Yang, Rational Design of Hydrogen Evolution Reaction Electrocatalysts for Commercial Alkaline Water Electrolysis, *Small Struct.*, 2023, **4**, 2200404.

7 R. Iwata, L. Zhang, K. L. Wilke, S. Gong, M. He, B. M. Gallant and E. N. Wang, Bubble growth and departure modes on wettable/non-wettable porous foams in alkaline water splitting, *Joule*, 2021, **5**, 887–900.

8 Z. Xie, D. Chen, J. Zhai, Y. Huang and H. Ji, Charge separation via synergy of homojunction and electrocatalyst in $BiVO_4$ for photoelectrochemical water splitting, *Appl. Catal., B*, 2023, **334**, 122865.

9 J. Zhang, T. Tang, Z. Xie, Y.-x. Chen, H. Yang, K.-H. Ye, J. Chen, W. Zou, J. Shi and Y. Huang, Polypyrrole as photothermal-assisted modifier for $BiVO_4$ photoanode enables high-performance photoelectrochemical water splitting, *Chem. Eng. J.*, 2024, **497**, 154833.

10 C. Zhang, W. Xu, S. Li, X. Wang, Z. Guan, M. Zhang, J. Wu, X. Ma, M. Wu and Y. Qi, Core-shell heterojunction engineering of $Ni_{0.85}Se$-O/CN electrocatalyst for efficient OER, *Chem. Eng. J.*, 2023, **454**, 140291.

11 X. Jing, Y. Mu, Z. Gao, X. Dong, C. Meng, C. Huang and Y. Zhang, Intermetallic ferric nickel silicide alloy derived from magadiite by magnesiothermic reaction as bifunctional electrocatalyst for overall water splitting, *Nano Res. Energy*, 2024, **3**, e9120104.

12 Z. Han, Y. Zhang, T. Lv, X. Tan, Q. Wang, Y. Wang and C. Meng, Core-shell cobalt-iron silicide electrocatalysts with enhanced bifunctional performance in hydrogen and oxygen evolution reactions, *J. Colloid Interface Sci.*, 2025, **682**, 1–10.

13 W. Li, Y. Liu, A. Azam, Y. Liu, J. Yang, D. Wang, C. C. Sorrell, C. Zhao and S. Li, Unlocking Efficiency: Minimizing Energy Loss in Electrocatalysts for Water Splitting, *Adv. Mater.*, 2024, **36**, 2404658.

14 G. V. Fortunato, E. Pizzutilo, I. Katsounaros, D. Göhl, R. J. Lewis, K. J. J. Mayrhofer, G. J. Hutchings, S. J. Freakley and M. Ledendecker, Analysing the relationship between the fields of thermo- and electrocatalysis taking hydrogen peroxide as a case study, *Nat. Commun.*, 2022, **13**, 1973.

15 Y. Mu, T. Wang, J. Zhang, C. Meng, Y. Zhang and Z. Kou, Single-Atom Catalysts: Advances and Challenges in Metal-Support Interactions for Enhanced Electrocatalysis, *Electrochem. Energy Rev.*, 2022, **5**, 145–186.

16 J. N. Hansen, H. Prats, K. K. Toudahl, N. Mørch Secher, K. Chan, J. Kibsgaard and I. Chorkendorff, Is There Anything Better than Pt for HER?, *ACS Energy Lett.*, 2021, **6**, 1175–1180.

17 M. A. Qadeer, X. Zhang, M. A. Farid, M. Tanveer, Y. Yan, S. Du, Z.-F. Huang, M. Tahir and J.-J. Zou, A review on fundamentals for designing hydrogen evolution electrocatalyst, *J. Power Sources*, 2024, **613**, 234856.

18 J. Zhu, S. Li, Z. Zhuang, S. Gao, X. Hong, X. Pan, R. Yu, L. Zhou, L. V. Moskaleva and L. Mai, Ultrathin Metal Silicate Hydroxide Nanosheets with Moderate Metal–Oxygen Covalency Enables Efficient Oxygen Evolution, *Energy Environ. Mater.*, 2022, **5**, 231–237.

19 Y. Zhang, X. Tan, Z. Han, Y. Wang, H. Jiang, F. Zhang, X. Zhu, C. Meng and C. Huang, Dual modification of cobalt silicate nanobelts by Co_3O_4 nanoparticles and phosphorization boosting oxygen evolution reaction properties, *J. Colloid Interface Sci.*, 2025, **679**, 1036–1045.

20 Y. Mu, Y. Zhang, X. Pei, X. Dong, Z. Kou, M. Cui and C. Meng, Dispersed FeO_x nanoparticles decorated with Co_2SiO_4 hollow spheres for enhanced oxygen evolution reaction, *J. Colloid Interface Sci.*, 2022, **611**, 235–245.

21 X. Pei, S. Yi, Y. Zhao, Y. Mu, Y. Yu, M. Cui, C. Meng, C. Huang and Y. Zhang, Nickel Oxide Nanoparticles Dispersed on Biomass–derived Amorphous Carbon/Cobalt Silicate Support Accelerate the Oxygen Evolution Reaction, *J. Colloid Interface Sci.*, 2022, **616**, 476–487.

22 X. Pei, Y. Zhang, Y. Mu, M. Cui, F. Tian and C. Meng, Cobalt oxide decorated three-dimensional amorphous carbon/cobalt silicate composite derived from bamboo leaves enables the enhanced oxygen evolution reaction, *Chem. Eng. Sci.*, 2022, **251**, 117490.

23 C. Ding, Y. Yu, Y. Wang, Y. Mu, X. Dong, C. Meng, C. Huang and Y. Zhang, Phosphate-modified Cobalt Silicate Hydroxide with Improved Oxygen Evolution Reaction, *J. Colloid Interface Sci.*, 2023, **648**, 251–258.

24 Y. Mu, Y. Zhang, Z. Feng, X. Dong, X. Jing, X. Pei, Y. Zhao, Z. Kou and C. Meng, Bifunctional electrocatalyst junction engineering: CoP nanoparticles *in situ* anchored on $Co_3(Si_2O_5)_2(OH)_2$ nanosheets for highly efficient water splitting, *Chem. Eng. J.*, 2023, **460**, 141709.

25 X. Pei, Y. Mu, X. Dong, C. Ding, L. Xu, M. Cui, C. Meng and Y. Zhang, Ion-change promoting Co nanoparticles@N-doped carbon framework on Co_2SiO_4/rGO support forming "double-triple-biscuit" structure boosts oxygen evolution reaction, *Carbon Neutralization*, 2023, **2**, 115–126.

26 Y. Mu, X. Pei, Y. Zhao, X. Dong, Z. Kou, M. Cui, C. Meng and Y. Zhang, In situ confined vertical growth of $Co_{2.5}Ni_{0.5}Si_2O_5(OH)_4$ nanoarrays on rGO for an efficient oxygen evolution reaction, *Nano Mater. Sci.*, 2023, **5**, 351–360.

27 T. M. El-Shamy and C. G. Pantano, Decomposition of silicate glasses in alkaline solutions, *Nature*, 1977, **266**, 704–706.

28 S. Onajah, R. Sarkar, M. S. Islam, M. Lalley, K. Khan, M. Demir, H. N. Abdelhamid and A. A. Farghaly, Silica-Derived Nanostructured Electrode Materials for ORR, OER, HER, CO2RR Electrocatalysis, and Energy Storage Applications: A Review, *Chem. Rec.*, 2024, **24**, e202300234.

29 C. A. Downes, K. M. Van Allsburg, S. A. Tacey, K. A. Unocic, F. G. Baddour, D. A. Ruddy, N. J. LiBretto, M. M. O'Connor, C. A. Farberow, J. A. Schaidle and S. E. Habas, Controlled Synthesis of Transition Metal Phosphide Nanoparticles to Establish Composition-Dependent Trends in Electrocatalytic Activity, *Chem. Mater.*, 2022, **34**, 6255–6267.

30 S. K. T. Aziz, S. Sultana, A. Kumar, S. Riyajuddin, M. Pal and A. Dutta, Transition metal phosphides as cardinal electrocatalytic materials for alkaline hydrogen production, *Cell Rep. Phys. Sci.*, 2023, **4**, 101747.

31 M. F. Delley, Z. Wu, M. E. Mundy, D. Ung, B. M. Cossairt, H. Wang and J. M. Mayer, Hydrogen on Cobalt Phosphide, *J. Am. Chem. Soc.*, 2019, **141**, 15390–15402.

32 A. A. Alothman, J. H. Shah, M. Un Nisa, S. Mohammad, A. G. Abid, M. Usman and M. Adnan, Integrated iron phosphides and cobalt oxide electrocatalyst for enhanced hydrogen and oxygen evolution reactions: A study on activity and stability factors, *Int. J. Hydrogen Energy*, 2024, DOI: **10.1016/j.ijhydene.2024.05.449**.

33 M. I. Díez-García, A. A. García Blanco, S. Murcia-López, M. Botifoll, J. Arbiol, M. Qamar and J. R. Morante, Flexible and Binder-Free Iron Phosphide Electrodes Using a Three-Dimensional Support for High Hydrogen Productivity, *ChemElectroChem*, 2023, **10**, e202201152.

34 J. Yin, J. Jin, Z. Yin, L. Zhu, X. Du, Y. Peng, P. Xi, C.-H. Yan and S. Sun, The built-in electric field across FeN/Fe_3N interface for efficient electrochemical reduction of CO_2 to CO, *Nat. Commun.*, 2023, **14**, 1724.

35 J. Wu, X. Gao and Z. Chen, Elucidating the construction and modulation of built-in electric field in the oxygen evolution reaction, *Chem. Eng. J.*, 2024, **492**, 152241.

36 Z. Feng, F. Lu, Q. Hu, J. Qiu, X. Lei, B. Wang, R. Guo, Y. Tian, X. Liu and J. You, Built-in electric fields and extra electric fields in the oxygen evolution reaction, *J. Mater. Chem. A*, 2024, **12**, 18047–18070.

37 H. Li, C. Guo, Y. Xiong and Y. Yang, Electric field induced band modulation of WS_2-GeC heterostructures for efficient photocatalytic water splitting: A density functional theory study, *Mater. Chem. Phys.*, 2020, **244**, 122732.

38 G. Meng, Z. Chang, L. Zhu, C. Chen, Y. Chen, H. Tian, W. Luo, W. Sun, X. Cui and J. Shi, Adsorption Site Regulations of [W–O]-Doped CoP Boosting the Hydrazine Oxidation-Coupled Hydrogen Evolution at Elevated Current Density, *Nano–Micro Lett.*, 2023, **15**, 212.

39 X. Dong, Y. Yu, X. Jing, H. Jiang, T. Hu, C. Meng, C. Huang and Y. Zhang, Sandwich-like honeycomb Co_2SiO_4/rGO/honeycomb Co_2SiO_4 structures with enhanced electrochemical properties for high-performance hybrid supercapacitor, *J. Power Sources*, 2021, **492**, 229643.

40 Z. Gu, X. Wei, X. Zhang, Z. Duan, Z. Gu, Q. Gong and K. Luo, Bimetallic-MOF-Derived Amorphous Zinc/Cobalt–Iron-Based Hollow Nanowall Arrays via Ion Exchange for Highly Efficient Oxygen Evolution, *Small*, 2021, **17**, 2104125.

41 X. Dong, X. Jing, Y. Mu, Y. Yu, C. Miao, C. Meng, C. Huang and Y. Zhang, Rational design of double-sandwich-like C@Co,CoO/Co_2SiO_4/rGO architectures boost electrochemical performances of Co_2SiO_4 for energy storage devices, *Chem. Eng. J.*, 2022, **431**, 133277.

42 Y. Zhang, C. Wang, X. Dong, H. Jiang, T. Hu, C. Meng and C. Huang, Alkali Etching Metal Silicates Derived from Bamboo Leaves with Enhanced Electrochemical Properties

for Solid-state Hybrid Supercapacitors, *Chem. Eng. J.*, 2021, **417**, 127964.

43 H. Yang, S. Hu, H. Zhao, X. Luo, Y. Liu, C. Deng, Y. Yu, T. Hu, S. Shan, Y. Zhi, H. Su and L. Jiang, High-performance Fe-doped ZIF-8 adsorbent for capturing tetracycline from aqueous solution, *J. Hazard. Mater.*, 2021, **416**, 126046.

44 Y. Chen, S. Hu, F. Nichols, F. Bridges, S. Kan, T. He, Y. Zhang and S. Chen, Carbon aerogels with atomic dispersion of binary iron–cobalt sites as effective oxygen catalysts for flexible zinc–air batteries, *J. Mater. Chem. A*, 2020, **8**, 11649–11655.

45 A. S. AlShammari, M. M. Halim, F. K. Yam and N. H. M. Kaus, Effect of precursor concentration on the performance of UV photodetector using TiO_2/reduced graphene oxide (rGO) nanocomposite, *Results Phys.*, 2020, **19**, 103630.

46 X. Tan, X. Dong, F. Zhang, C. Huang and Y. Zhang, Structure engineering of nickel silicate/carbon composite with boosted electrochemical performances for hybrid supercapacitors, *J. Colloid Interface Sci.*, 2024, **674**, 67–78.

47 N. Dwivedi, S. Kumar, H. K. Malik, Govind, C. M. S. Rauthan and O. S. Panwar, Correlation of sp3 and sp2 fraction of carbon with electrical, optical and nanomechanical properties of argon-diluted diamond-like carbon films, *Appl. Surf. Sci.*, 2011, **257**, 6804–6810.

48 Z. Huang, Q. Zhou, J. Wang and Y. Yu, Fermi-level-tuned MOF-derived N-ZnO@NC for photocatalysis: A key role of pyridine-N-Zn bond, *J. Mater. Sci. Technol.*, 2022, **112**, 68–76.

49 Y. Luo, H. Yang, P. Ma, S. Luo, Z. Zhao and J. Ma, Fe_3O_4/CoO Interfacial Nanostructure Supported on Carbon Nanotubes as a Highly Efficient Electrocatalyst for Oxygen Evolution Reaction, *ACS Sustainable Chem. Eng.*, 2020, **8**, 3336–3346.

50 Y. Zhao, L. Zheng, H. Wu, H. Chen, L. Su, L. Wang, Y. Wang and M. Ren, Co_2SiO_4/SiO_2/RGO nanosheets: Boosting the lithium storage capability of tetravalent Si by using highly-dispersed Co element, *Electrochim. Acta*, 2018, **282**, 609–617.

51 K. Zhu, F. Shi, X. Zhu and W. Yang, The roles of oxygen vacancies in electrocatalytic oxygen evolution reaction, *Nano Energy*, 2020, **73**, 104761.

52 J. Shi, F. Qiu, W. Yuan, M. Guo and Z.-H. Lu, Nitrogen-doped carbon-decorated yolk-shell CoP@FeCoP micro-polyhedra derived from MOF for efficient overall water splitting, *Chem. Eng. J.*, 2021, **403**, 126312.

53 Y. Feng, C. Xu, E. Hu, B. Xia, J. Ning, C. Zheng, Y. Zhong, Z. Zhang and Y. Hu, Construction of hierarchical FeP/Ni_2P hollow nanospindles for efficient oxygen evolution, *J. Mater. Chem. A*, 2018, **6**, 14103–14111.

54 R. Boppella, J. Tan, W. Yang and J. Moon, Homologous CoP/NiCoP Heterostructure on N-Doped Carbon for Highly Efficient and pH-Universal Hydrogen Evolution Electrocatalysis, *Adv. Funct. Mater.*, 2019, **29**, 1807976.

55 S. Niu, W.-J. Jiang, Z. Wei, T. Tang, J. Ma, J.-S. Hu and L.-J. Wan, Se-Doping Activates FeOOH for Cost-Effective and Efficient Electrochemical Water Oxidation, *J. Am. Chem. Soc.*, 2019, **141**, 7005–7013.

56 L. Gao, S. Chang and Z. Zhang, High-Quality CoFeP Nanocrystal/N, P Dual-Doped Carbon Composite as a Novel Bifunctional Electrocatalyst for Rechargeable Zn–Air Battery, *ACS Appl. Mater. Interfaces*, 2021, **13**, 22282–22291.

57 Y. Duan, Z.-Y. Yu, S.-J. Hu, X.-S. Zheng, C.-T. Zhang, H.-H. Ding, B.-C. Hu, Q.-Q. Fu, Z.-L. Yu, X. Zheng, J.-F. Zhu, M.-R. Gao and S.-H. Yu, Scaled-Up Synthesis of Amorphous NiFeMo Oxides and Their Rapid Surface Reconstruction for Superior Oxygen Evolution Catalysis, *Angew. Chem., Int. Ed.*, 2019, **58**, 15772–15777.

58 S. Kundu, B. Malik, A. Prabhakaran, D. K. Pattanayak and V. K. Pillai, Topotactic transition of α-$Co(OH)_2$ to β-$Co(OH)_2$ anchored on CoO nanoparticles during electrochemical water oxidation: synergistic electrocatalytic effects, *Chem. Commun.*, 2017, **53**, 9809–9812.

59 J. S. Kim, I. Park, E.-S. Jeong, K. Jin, W. M. Seong, G. Yoon, H. Kim, B. Kim, K. T. Nam and K. Kang, Amorphous Cobalt Phyllosilicate with Layered Crystalline Motifs as Water Oxidation Catalyst, *Adv. Mater.*, 2017, **29**, 1606893.

60 L. Yu, J. F. Yang, B. Y. Guan, Y. Lu and X. W. Lou, Hierarchical Hollow Nanoprisms Based on Ultrathin Ni-Fe Layered Double Hydroxide Nanosheets with Enhanced Electrocatalytic Activity towards Oxygen Evolution, *Angew. Chem., Int. Ed.*, 2018, **57**, 172–176.

61 Y. Men, P. Li, F. Yang, G. Cheng, S. Chen and W. Luo, Nitrogen-doped CoP as robust electrocatalyst for high-efficiency pH-universal hydrogen evolution reaction, *Appl. Catal., B*, 2019, **253**, 21–27.

62 H. Ma, Z. Chen, Z. Wang, C. V. Singh and Q. Jiang, Interface Engineering of Co/CoMoN/NF Heterostructures for High-Performance Electrochemical Overall Water Splitting, *Adv. Sci.*, 2022, **9**, 2105313.

63 J.-X. Feng, S.-Y. Tong, Y.-X. Tong and G.-R. Li, Pt-like Hydrogen Evolution Electrocatalysis on PANI/CoP Hybrid Nanowires by Weakening the Shackles of Hydrogen Ions on the Surfaces of Catalysts, *J. Am. Chem. Soc.*, 2018, **140**, 5118–5126.

64 N. Cheng, L. Ren, X. Xu, Y. Du and S. X. Dou, Recent Development of Zeolitic Imidazolate Frameworks (ZIFs) Derived Porous Carbon Based Materials as Electrocatalysts, *Adv. Energy Mater.*, 2018, **8**, 1801257.

65 R. Balu, X. Zhong, R. Pandey and S. P. Karna, Effect of electric field on the band structure of graphene/boron nitride and boron nitride/boron nitride bilayers, *Appl. Phys. Lett.*, 2012, **100**, 052104.

66 X. Tan, F. Zhang, D. Chen, P. Wang, Y. Liu, C. Meng and Y. Zhang, Modulating NH_4^+ in vanadium oxide framework for high-efficient aqueous NH_4^+ storage, *Chem. Eng. J.*, 2024, **489**, 151119.

67 X. Ma, X. Cao, M. Yao, L. Shan, X. Shi, G. Fang, A. Pan, B. Lu, J. Zhou and S. Liang, Organic–Inorganic Hybrid Cathode with Dual Energy-Storage Mechanism for Ultrahigh-Rate and Ultralong-Life Aqueous Zinc-Ion Batteries, *Adv. Mater.*, 2022, **34**, 2105452.